Global Ionospheric Electron Density from GNSS-POD Limb Measurements

Dong L. Wu[1], Nimalan Swarnalingam[1,2], Cornelius Csar Jude H. Salinas[1,3], Daniel J. Emmons[4], and Tyler C. Summers[1,5]

(1) NASA Goddard Space Flight Center, Greenbelt, Maryland, USA, dong.l.wu@nasa.gov; (2) The Catholic University of America, Washington DC, USA, swarnalingam@cua.edu; (3) GESTAR-2 University of Maryland Baltimore County, Baltimore, Maryland, USA; (4) The Air Force Institute of Technology, Wright-Patterson AFB, Ohio, USA; daniel.emmons@afit.edu; (5) Science Systems and Applications Inc., Lanham, Maryland, USA, tyler.summers@nasa.gov

Abstract

GNSS-LEO radio links from Precise Orbital Determination (POD) and Radio Occultation (RO) antennas have been used increasingly in studying and monitoring the global ionospheric electron density (N_e). In this study we developed an optimal estimation (OE) method to retrieve Ne profiles from the slant total electron content (*hTEC*) measurements acquired by the GNSS-POD links at negative elevation angles. The hmF2 and NmF2 from the OE retrieval are validated against ground-based ionosondes and radar observations, showing generally good agreements in NmF2 from all sites. Nighttime hmF2 measurements tend to agree better than the daytime when the ionosonde heights tend to be slightly lower. The OE algorithm has been applied to all GNSS-POD data acquired from the COSMIC-1 (2006-2019), COSMIC-2 (2019-present), and Spire (2019-present) constellations, showing a consistent ionospheric N_e morphology. A detailed analysis of the frequency-wavenumber spectra is made for the N_e variability at different heights. In the lower ionosphere (~150 km) we found significant spectral power in DE1, DW6, DW4, SW5, and SE4 wave components, in addition to well-known DW1, SW2 and DE3 waves. In the upper ionosphere (~450 km), additional wave components are still present, including DE4, DW4, DW6, SE4 and SW4. The co-exist of eastward and westward propagating WN4 components implies the presence of a stationary planetary wave4 (sPW4), as suggested by other earlier studies.

1 Introduction

GNSS remote sensing on low-Earth-orbit (LEO) satellites is often equipped with two types of receiver antennas, Precise Orbital Determination (POD) and Radio Occultation (RO). COSMIC-2, for example, have two sets of these receivers situated in the fore and aft directions with respect to the satellite orbital plane [Fig.1]. The POD antennas are often designed with a low-gain, wide field-of-view (FOV) with a 1-Hz sampling rate in GNSS-POD links, whereas the RO antennas have a high-gain, narrow FOV with a 50/100-Hz sampling rate in GNSS-RO links.

Both GNSS-POD and GNSS-RO links can be affected by ionospheric N_e, which induces a phase delay of radio wave propagation. As shown in Fig.1, the GNSS-RO links have negative elevation angles ($\varepsilon < 0°$), but the GNSS-POD

links can have both positive and negative ε angles. Both GNSS-POD and GNSS-RO measurements at $\varepsilon < 0°$ can be used for limb sounding of the ionosphere, but the GNSS-POD data have a more complete coverage of the F-region ionosphere [Fig.1].
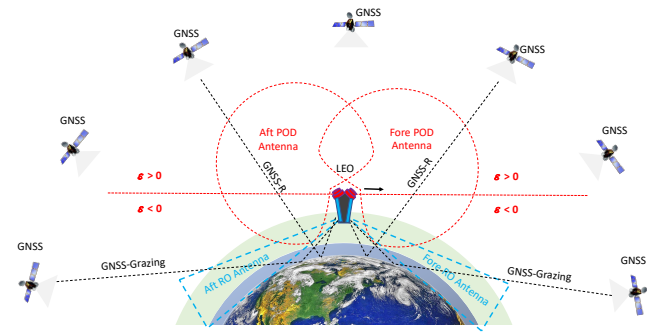

Fig.1. A schematic to show two sets of the POD (red) and RO (cyan) L-band receiver antennas on a LEO satellite (center box) with the fore and aft views in the flight direct (arrow). Their antenna patterns are drawn by circular (red) and triangle (cyan) lines to indicate a wide and narrow FOV respectively. Both POD and RO antennas can be used for limb sounding from the measurements at negative elevation angles ($\varepsilon < 0°$). The horizontal dashed line denotes $\varepsilon = 0°$. The POD and RO antennas can also be modified to receive the GNSS signals from a sharp reflection angle (GNSS-R) and a grazing angle (GNSS-Grazing).

2 Data and Method

2.1 *hTEC* Limb Profiles

The horizontally integrated total electron content, or *hTEC*, is a function of tangent height h_t between GNSS and LEO satellites. The *hTEC* of GNSS-POD and GNSS-RO links can be derived from the excess phase measurements (ϕ_{exL1} and ϕ_{exL2}) at L1 (f_1=1.57542 GHz) and L2 (f_2=1.22760 GHz) frequencies by

$$hTEC = (\phi_{exL1} - \phi_{exL2}) \frac{f_1^2 f_2^2}{40.3 \times 10^{16}(f_2^2 - f_1^2)} \qquad (1)$$

Ionospheric bending is neglected in this calculation, since it is a secondary effect compared to the phase advance induced the ionospheric plasma. As a key input for the N_e inversion, $hTEC(h_t)$ is an integral along the GNSS-LEO link and can be expressed by

$$hTEC(h_t) = \int_{LEO}^{GNSS} N_e \cdot ds$$

$$= \int_{h_t}^{Z_{GNSS}} N_e(z) \cdot z / \sqrt{z^2 - h_t^2}\, dz +$$

$$\int_{Z_{LEO}}^{h_t} N_e(z) \cdot z / \sqrt{z^2 - h_t^2}\, dz \qquad (2)$$

where Z_{LEO} is the LEO satellite altitude, and Z_{GNSS} is the GNSS satellite altitude. The term, $z \cdot dz / \sqrt{z^2 - h_t^2}$, is known as the Abel weighting function. Z_{GNSS} is high enough above the ionosphere and $Z_{GNSS} \approx \infty$ is a good approximation. With respect to the receiver on LEO, the first integral is from the far side of the tangent point whereas the second integral is from the near side. Although the LEO position may change significantly, the tangent points of limb profile do not move much.

The absolute *hTEC* calibration at $\varepsilon < 0$ is required for the N_e retrieval. Because the *hTEC* measurement is derived from the pseudorange of GNSS-LEO links, its navigation error is typically 1-3m [1], which corresponds to 6-18 TECu. The *podTEC* files produced by CDAAC and Spire contain vertical *TEC* (*vTEC*) from the measurements at $\varepsilon > 0$, which is the *TEC* above the satellite altitude converted from *hTEC* using $\sin(\varepsilon)$. However, most of the CDAAC *podTEC* files do not have *hTEC* at $\varepsilon < 0$ except for COSMIC-1 and COSMIC-2. On the other hand, the Spire *hTEC* product under NASA's Commercial Smallsat Data Acquisition (CSDA) has measurements for $\varepsilon < 0$ but they are not calibrated. Forsythe et al. [2] proposed a mitigation solution that uses the differential *hTEC* quantity, D*hTEC* = *hTEC*(-ε) – *hTEC*(ε), and assumes the far- and near-side *hTEC*(ε) are same. This assumption, however, can induce another error for *hTEC* that are sometimes significant especially in the situation where there is a strong horizontal N_e gradient.

In this study we developed an empirical method for *hTEC* calibration, by taking advantage of a nearly universal linear relationship between the limb-viewing *hTEC* and its vertical gradient in the top side of the ionosphere. If satellites fly inside the ionosphere and make limb measurements with the GNSS-LEO link, there is a good linear relationship between the observed *hTEC* and its vertical derivative at ε between -2° and -10°. Because the low flying LEO satellites only observe part of the ionosphere, it is challenging to obtain a good absolute calibration for both *hTEC* (or pseudorange) and the LEO POD from a single link. Solving both variables accurately would require a least-squared solution to the measurements from multiple links. Thus, this approach with the empirical linear relationships can provide an effective calibration of *hTEC* as an *ad-hoc* near-real-time (NRT) processing.

2.2 Inversion algorithm

The N_e inversion problem is formulated with the same optimal estimation (OE) method as described in Wu et al. [3]. The input measurement vector **y** is the calibrated *hTEC* related to as N_e (Eq.2) as a function of h_t, i.e., $\mathbf{y} \equiv \{hTEC(h_t); h_t = h_1 \cdots h_{max}\}$ where h_{max} is the maximum h_t below Z_{sat}. The state vector **x** is N_e profile, i.e., $\mathbf{x} \equiv \{N_e(z); z = 100\, km, \cdots, z_{max}\}$. For the *F*-region N_e retrieval, z_{max} is set at 800 km and the inverted $N_e(z)$ profile above Z_{sat} is essentially an extrapolation with the information from the upper tail of Abel weighting functions.

We use a linearized forward model for the measurement vector (**y**) and the state vector (**x**) that are related by the weighting function **K**, or the *Jacobians* as in $\mathbf{K} = \partial\mathbf{y}/\partial\mathbf{x}$, as follows

$$\mathbf{y} = \mathbf{y_0} + \mathbf{K} \cdot (\mathbf{x} - \mathbf{x_0}) + \boldsymbol{\varepsilon_y} \qquad (3)$$

where the linearization state vector is $\mathbf{x_0}$ (N_e in m^{-3}) and the associated measurement vector $\mathbf{y_0}$ (*hTEC* in TECu). The model is linearized on a single state vector $\mathbf{x_0}$, which is the annual mean of the 2008 International Reference Ionosphere (IRI)-2016 in the *F*-region [4] and the mean Faraday-IRI (FIRI) in the *E*-region [5] for a solar minimum condition.

The spherical homogeneity assumption is used in the current version (V6p) of the OE algorithm, in which the Abel weighting function **K** and the inverted profile **x** are at the tangent point location. The algorithm parameters used for the *F*-region N_e retrieval are similar to those in the similar version (V4) of the *E*-region retrieval [3], with a measurement uncertainty (2 TECu) added to measurement vector **y**, or $\boldsymbol{\varepsilon_y}$. The **x** inversion in the optimal estimation method [6] can be expressed by

$$\hat{\mathbf{x}} = \left[\mathbf{S_a^{-1}} + \mathbf{K}^T \mathbf{S_y^{-1}} \mathbf{K}\right]^{-1} \left[\mathbf{S_a^{-1}} \mathbf{a} + \mathbf{K}^T \mathbf{S_y^{-1}} \mathbf{y}\right] \qquad (4)$$

$$\mathbf{S_{\hat{x}}} = \left[\mathbf{S_a^{-1}} + \mathbf{K}^T \mathbf{S_y^{-1}} \mathbf{K}\right]^{-1} \qquad (5)$$

where $\hat{\mathbf{x}}$ is an optimal solution to **x** in Eq.3 with its uncertainty determined by $\mathbf{S_{\hat{x}}}$. **a** is the *a priori* of **x**, which is set to be same as $\mathbf{x_0}$ in this study. $\mathbf{S_a} = \varepsilon_{x0}^2 \cdot \boldsymbol{I}$ and $\mathbf{S_y} = \varepsilon_y^2 \cdot \boldsymbol{I}$ are covariance matrices for **a** and **y** respectively. Like in the V4 *E*-region retrieval, $\mathbf{S_a}$ is empirically determined to allow a stable inversion for the large N_e dynamic range and variability with respect to altitude. Both $\mathbf{x_0}$ and $\boldsymbol{\varepsilon_{x0}}$ profiles are depicted.

3 Results

The OE algorithm has been applied to all COSMIC-1, COSMIC-2, Spire and other GNSS-POD data that have *hTEC* measurements with $\varepsilon < 0$. Most of these data were obtained from at the CDAAC distribution, except for Spire. The latter is obtained from the NASA CSDA program. The *hTEC* data from CDAAC have a pseudorange calibration. In addition, CDAAC also provides the *F*-region N_e retrieval in COSMIC-1 and COSMIC-2 level-2 data (ionPrf).

The V6p N_e and CDAAC N_e (ionPrf) profiles generally agree with each other at the topside of the *F*-layer. However, large differences are seen in its bottom side and in the *E*-region. Strong diurnal variations of the *F*-region N_e provide a good test or validation to the retrieval

sensitivity. As shown in Fig.2, the V6p OE algorithm produces N_e values that agrees generally well with the IRI-2016 model. The daytime retrievals show values of an order of amplitude greater than the linearization point, despite the single state vector used. The diurnal variation appears to be captured at all altitudes. The diurnal variations at the selected altitudes in the F-region compare reasonably well, in terms of hourly means, with the N_e retrievals from CDAAC data that applied a very different approach to the inversion problem.

The zonal mean N_e distribution from July 2022 reveals a 2-hourly climatology from the Spire constellation can provide for characterizing the ionosphere. With the stable inversion algorithm from the OE method, the E-to-F-region transition of global N_e distribution across the meridional plane is readily seen in different local times. The F_1-layer (140-200 km) can be recognized in the F-region during daytime as soon as the Sun rises. This layer is the most interesting for long-distance communications and has a similar behavior to the E-layer. The F_1-layer does not disappear rapidly in the evening hours after sunset, as it remains ionized till midnight before merging with the F_2-layer. The latitude-dependent F_1-layer N_e distribution is evident the morning and evening hours.
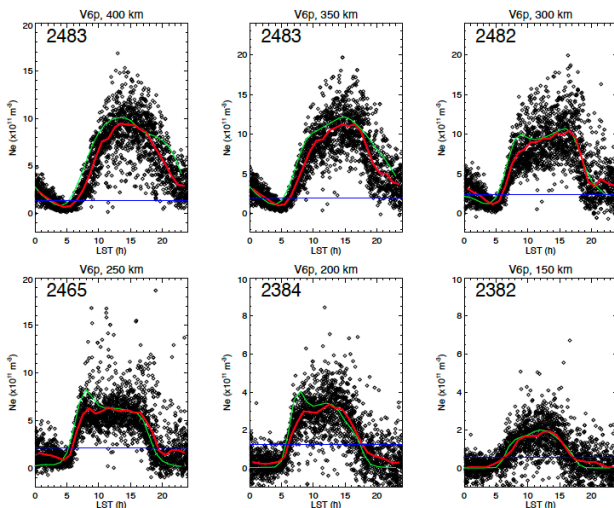

Fig.2. The V6p retrievals of COSMIC-2 N_e at six height levels (150, 200, 250, 300, 350 and 400 km) from the tropics (10°S-10°N) on December 1, 2021. The IRI-2016 model is the green line. The blue straight line is the linearization state vector $\mathbf{x_0}$ and the red line is the hourly mean of COSMIC-2 N_e. The number of valid retrievals is indicated in each height panel.

The so-called equatorial "fountain effect" is clear seen in daytime zonal means when the vertical $\mathbf{E}$x$\mathbf{B}$ drift lifts the plasma to a higher altitude [Fig.3]. A double-peak structure is evident at LT=21h as the plasma redistributes along the magnetic field lines from the equator to higher latitudes. Atmospheric tides and planetary waves can modulate the $\mathbf{E}$x$\mathbf{B}$ drift considerably, creating significant longitudinal and local time variations to the fountain effect [7][8].
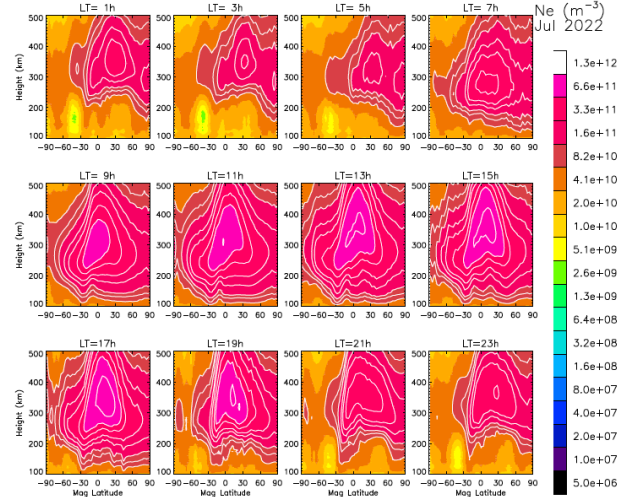

Fig.3. Spire monthly zonal mean N_e as a function of magnetic latitude and local time (LT) for July 2022. A 2-hourly LT bin is used to produce good statistics from the Spire constellation. The 3U CubeSats from the Spire constellation were mostly operated at an orbital altitude below 525 km.

Equatorial ionization anomaly (EIA) is a salient ionospheric structure along the geomagnetic equatorial band (15°S-15°N). It shows a persistent wavenumber-4 (WN4) feature in zonal winds [9], UV emissions [7], and ionospheric peak density NmF2 [10]. The longitudinal variation is thought due to the dynamo interaction between the tides with the daytime lower ionosphere (E-layer). The WN3 eastward-propagating non-migrating diurnal tide (DE3), induced by the tropospheric forcing, has been suggested as a primary tidal component that is responsible for the WN4 variation [11]. However, other wave components can also contribute the apparent WN4 structure, including the semidiurnal eastward-propagating WN2 semidiurnal tide (SE2) and the stationary planetary wave4 (sPW4) [12][13]. In the following we follow the normal naming convention [13], to express ionospheric oscillations as

$$A_{n,s} \cdot \cos\left(n\Omega t + s\lambda - \phi_{n,s}\right) \qquad (6)$$

where t is universal time, Ω is the Earth rotation rate, λ is longitude, n is a subharmonic of a day, and s is zonal wavenumber with negative values indicating the eastward propagation. $A_{n,s}$ and $\phi_{n,s}$ are the amplitude and phase of wave component (n,s), respectively. Wave components (n,s) are also named by letters with 'D', 'S', and 'T' for diurnal, semidiurnal and terdiurnal oscillations, and 'E' and 'W' as eastward and westward propagating waves. For example, the migrating diurnal tide is (1,1) or DW1, and the non-migrating eastward-propagating WN3 diurnal tide is (1,-3) or DE3.

Here we conducted a frequency-wavenumber spectral analysis for the N_e data retrieved from the GNSS-POD measurements. Because the EIA is highly modulated by the magnetic field, we chose to carry out the spectral analysis along the geomagnetic tropics (10°S-10°N), instead of the geographic tropics, to focus on longitudinal variations

along the constant magnetic dip angles. Fig.4 compares the frequency-wavenumber spectra scanned from the Spire and COSMIC-2 N_e measurements in Jan 2022 from the magnetic tropics. Despite different spatiotemporal sampling patterns between two constellations, their power spectra reveal a distribution similar to each other in terms of major wave components. The Spire spectra appear to be slightly noisier than the COSMIC-2, likely because its sampling in the tropics is sparser.
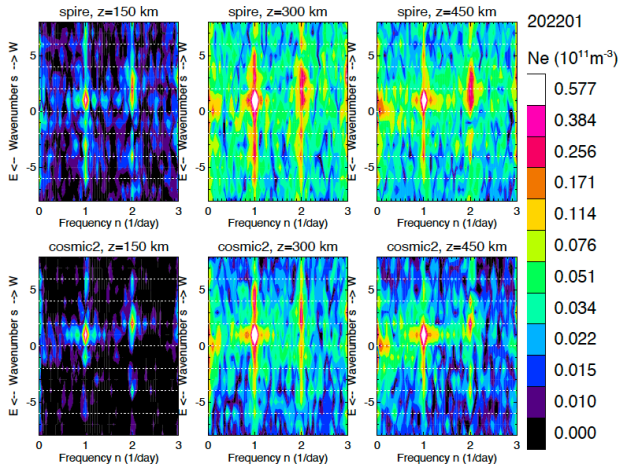

Fig.4 Frequency-wavenumber power spectra from Spire and COSMIC-2 N_e in Jan 2022 along the magnetic equator.

4 Summary

GNSS-LEO N_e measurements from the OE algorithm have showed great improvements in the ionosphere, which can used to characterize global 3D N_e distribution and variability. Although both OE and OP methods use the Abel weighting function in the N_e inversion, they are significantly different in terms of performance in the lower ionosphere. The new OE results can overcome the large N_e oscillations, sometimes negative values, seen in the OP retrievals in the E-region ionosphere.

The unprecedented spatiotemporal sampling of the ionosphere from the recent Spire and COSMIC-2 constellations allows a detailed analysis of the frequency-wavenumber spectra for the N_e variability at different heights. The WN4 components are found with a significant power in most seasons, in addition to the DW1, SW2 and DE3 modes previously studied.

Further improvements with the OE method include a tomographic inversion technique that leverages the asymmetric sampling about the tangent point associated with GNSS-LEO links.

Acknowledgements

References

[1] A. Hauschild, and O. Montenbruck. Precise real-time navigation of LEO satellites using GNSS broadcast ephemerides. NAVIGATION. 2021;68(2):419–432. https://doi.org/10.1002/navi.416.

[2] V. V. Forsythe, et al. (2020). Validation of ionospheric electron density measurements derived from Spire CubeSat constellation. Radio Sci, 55, e2019RS006953. https://doi.org/10.1029/2019RS006953

[3] D.L. Wu, D. J. Emmons, N. Swarnalingam, Global GNSS-RO Electron Density in the Lower Ionosphere. Remote Sens. 2022, 14, 1577. https://doi.org/10.3390/rs14071577

[4] D. Bilitza, et al. (2017), International Reference Ionosphere 2016: From ionospheric climate to real-time weather predictions, Space Weather, 15,418–429, doi:10.1002/2016SW001593

[5] M. Friedrich, et al. (2018). FIRI-2018, an updated empirical model of the lower ionosphere. Journal of Geophysical Research: Space Physics, 123, 6737–6751. https://doi.org/10.1029/ 2018JA025437.

[6] C. D. Rodgers, Inverse Methods for Atmospheric Sounding - Theory and Practice, SAOPP...2, 2000. doi:10.1142/9789812813718.

[7] T. J. Immel, et al. (2006), Control of equatorial ionospheric morphology by atmospheric tides, Geophys. Res. Lett., 33, L15108, doi:10.1029/2006GL026161.

[8] S. L. England, et al. (2010), Modeling of multiple effects of atmospheric tides on the ionosphere: An examination of possible coupling mechanisms responsible for the longitudinal structure of the equatorial ionosphere, J. Geophys. Res., 115, A05308, doi:10.1029/2009JA014894.

[9] H. K. Lu¨hr, et al. (2007), Longitudinal variation of F region electron density and thermospheric zonal wind caused by atmospheric tides, Geophys. Res. Lett., 34, L16102, doi:10.1029/2007GL030639

[10] A. N. Onohara, et al., Wavenumber-4 structures observed in the low-latitude ionosphere during low and high solar activity periods using FORMOSAT/COSMIC observations, Ann. Geophys., 36, 459–471, https://doi.org/10.5194/angeo-36-459-2018, 2018.

[11] J. M. Forbes, et al. (2006), Troposphere-thermosphere tidal coupling as measured by the SABER instrument on TIMED during July–September 2002, J. Geophys. Res., 111, A10S06, doi:10.1029/2005JA011492.

[12] N. M. Pedatella, et al. (2012), The comparative importance of DE3, SE2, and SPW4 on the generation of wavenumber-4 longitude structures in the low-latitude ionosphere during September equinox, Geophys. Res. Lett., 39, L19108, doi:10.1029/2012GL053643.

[13] J. M. Forbes, et al. (2008), Tidal variability in the ionospheric dynamo region, J. Geophys. Res., 113, A02310, doi:10.1029/2007JA012737.